Chemical Science

ROYAL SOCIETY OF CHEMISTRY

EDGE ARTICLE

View Article Online
View Journal | View Issue

Cite this: *Chem. Sci.*, 2025, **16**, 20601

All publication charges for this article have been paid for by the Royal Society of Chemistry

Identifying inorganic solids for harsh environments *via* machine learning

Jacob C. Hickey,[ab] Arman M. Karimaghaei,[a] Matt Flores,[a] Sally Hoang,[a] Roy Arrieta,[ab] Amit Kumar,[a] Gonzalo Cuervo,[a] Peter Zhu[a] and Jakoah Brgoch *[ab]

Received 31st July 2025
Accepted 27th September 2025

DOI: 10.1039/d5sc05800g

rsc.li/chemical-science

Developing multifunctional materials with superior mechanical properties, including high hardness and oxidation resistance, remains essential for aerospace, defense, and industrial applications. Machine learning offers a powerful, data-driven pathway for discovering new hard, oxidation-resistant materials for these uses, providing an efficient and scalable alternative to conventional materials discovery methods. Here, we present a pair of extreme gradient boosting (XGBoost) models, trained on compositional and structural descriptors. A Vickers hardness (H_V) model was developed using a curated dataset of 1225 while a model for predicting the oxidation temperature (T_p) was constructed using 348 compounds. The model was subsequently validated against a diverse dataset of 18 inorganic compounds, including borides, silicides, and intermetallics, with previously unmeasured oxidation temperatures. Integrating the updated structure-informed hardness model with the new oxidation model enabled the identification of multifunctional materials that simultaneously exhibit superior hardness and enhanced oxidation resistance. This work highlights the potential of machine learning to accelerate materials discovery and provides a robust framework for identifying compounds capable of withstanding extreme environments.

1. Introduction

Developing materials that resist oxidation at elevated temperatures while maintaining their mechanical properties (hardness) under harsh conditions is critical for advancing technologies in aerospace, energy, defense, and industrial manufacturing.[1] Traditional methods for developing oxidation-resistant materials remain costly and time-consuming often requiring multiple synthesis cycles, detailed characterization, and challenging scale-up.[2,3] To address these limitations, researchers are adopting more efficient and targeted strategies that can be used to discover new materials by modifying known systems through compositional tuning, forming composites,[4] and investigating underexplored and chemically complex phase spaces.[5,6]

Early efforts to accelerate the discovery of new structural materials relied on first-principles methods like density functional theory (DFT), which have transformed materials property predictions across diverse application spaces.[7] However, DFT often struggles to provide accurate quantitative predictions of specific mechanical properties, particularly oxidation resistance and hardness. Oxidation is a complex, dynamic, temperature-dependent process that extends beyond DFT's static, ground-state framework, involving gas-phase interactions, defect formation, and interfacial reactions. Furthermore, modeling idealized surfaces or perfect stoichiometries limits predictive reliability for real-world oxidation behavior. Likewise, hardness arises from complex deformation mechanisms, such as dislocation motion and grain boundary interactions, which are difficult to capture accurately with conventional DFT due to its limited treatment of long-range strain and non-equilibrium processes.

Machine learning offers a data-driven framework capable of overcoming many of these limitations by capturing complex relationships across composition, structure, processing, and functional properties. For example, prior studies demonstrated the utility of machine learning for predicting a range of thermal, electronic, and mechanical properties, including hardness,[8–10] elastic moduli,[11–14] creep,[15] fatigue,[16,17] and plastic deformation.[18–20] Our group previously developed a machine learning model for Vickers hardness (H_V) based solely on compositional descriptors, enabling the prediction of load-dependent hardness without requiring structural, microstructural, or processing information. This model has been used to quantitatively determine H_V for virtually any given composition, even large or disordered unit cells, *a priori*. Nevertheless, this initial approach could not distinguish between polymorphs and allotropes. Machine learning is also increasingly practical for predicting the oxidation behavior of materials. Recent studies

[a]*Department of Chemistry, University of Houston, Texas 77204, USA. E-mail: jbrgoch@central.uh.edu*

[b]*Texas Center for Superconductivity, University of Houston, Houston, Texas 77204, USA*

have shown that machine learning models outperform traditional methods in estimating oxide scale stability,[21] enabling the rapid screening of multicomponent oxide catalysts for oxygen reduction.[22] They have also shown promise in guiding the design of oxidation-resistant alloys, including high-entropy alloys[23] and Ni-based superalloys.[24] These advances highlight exciting progress in the field; however, most models remain limited in scope and are not easily generalized across compositional spaces and structural complexity.

Motivated by these studies, the work here introduces a machine learning framework that couples three predictive models to accelerate the discovery of multifunctional materials with high hardness and oxidation resistance. The first set of models predicts the bulk and shear moduli of compounds *via* an extreme gradient boosting (XGBoost) approach.[25] The predicted values are then incorporated as descriptors in a second model that extends our load-dependent Vickers microhardness with structural and compositional features. In parallel, we construct a third model that can predict the oxidation temperature of a material, using a similar integrated set of structural and compositional descriptors. This general oxidation model is trained on a dataset of 275 literature-reported compounds, expanded with 71 newly synthesized materials. This model was experimentally validated against 17 additional unreported compounds. Combining both models, the framework was applied to a screening set of 15 247 pseudo-binary and ternary compounds, yielding at least three candidates with high hardness and oxidation resistance. This work demonstrates the utility of structural descriptors in capturing complex materials behavior and highlights the potential of machine learning to accelerate the discovery of next-generation multifunctional materials.

2. Experimental section

2.1 Machine learning

Three distinct supervised machine learning models were developed in this work: a set of models for the bulk and shear moduli of compounds, another for the load-dependent hardness of inorganic materials, and a third for the oxidation temperature of inorganic materials. The bulk and shear moduli are subsequently predicted and used as descriptors in both the hardness and oxidation temperature predictions. Finally, pseudo-binary and ternary metal compounds extracted from the Materials Project dataset are screened to identify inorganic materials that exhibit high hardness and oxidation resistance. The optimized models, training data, and prediction sets are provided in the open-source GitHub repository at **https://github.com/BrgochGroup**.

2.1.1 Bulk and shear moduli model. First, a training dataset of binary and ternary compounds with calculated bulk and shear moduli was extracted from the Materials Project database.[26] This Materials Project employs a high-throughput workflow leveraging Density Functional Perturbation Theory[27] *via* the Vienna *ab Initio* Simulation Package (VASP) to calculate the elastic tensors.[28] The Perdew–Burke–Ernzerhof (PBE)[29] functional is applied for exchange–correlation processes, and the DFT + U approach (incorporating the Hubbard parameter) is adopted for systems with significant correlation.[30] The elastic tensors are converted into elastic constants (moduli) following the Voigt–Reuss–Hill approximation.[31]

The training dataset was meticulously re-cleaned, as outlined in our group's earlier work.[11] This involved discarding entries with negative or chemically unsensible bulk and shear moduli. Compounds containing noble gases were also eliminated. Additionally, compounds containing hydrogen, technetium (Tc), and elements with atomic numbers above 83, except uranium and thorium, were excluded. The final training dataset comprised 7148 compounds, more than doubling the size from our previous research.[11] Each compound's Materials project Task ID was also included to identify different polymorphs.

Two XGBoost models were then constructed to predict the bulk and shear moduli. This algorithm is a highly efficient and scalable method that leverages an ensemble of gradient-boosted decision trees.[32] XGBoost operates by successively incorporating weak learners to mitigate errors from preceding iterations, thereby resulting in a robust model that significantly enhances prediction accuracy through iterative variance and bias reduction.[25,33] Comprehensive information on feature generation and selection, hyperparameter optimization, and model training procedures is available in SI Section 1.1, including the complete list of features for the bulk and shear models (Tables S1 and S2). An analysis comparing the hyperparameter-optimized models developed here to our previous (SVM-based) work revealed that the XGBoost model performs slightly better, based on improved model statistics.[11]

2.1.2 Load dependent Vickers microhardness model. A new load dependent Vickers microhardness model was constructed that incorporates both structural and compositional information. The training dataset consists of 1225 H_V values from 606 distinct compounds. These data were obtained from literature and in-house microindentation experiments conducted under different applied loads. Care was taken to include Vickers hardness values from only bulk polycrystalline, rather than hardness data collected on single crystals or collected any other hardness measurement (*e.g.*, Knoop, Rockwell, *etc.*). Hardness values are not easily transferable due to fundamental differences between hardness techniques, the anisotropic nature of single-crystals, size effects like the Hall–Petch relationship, and inherent impurities and defects within polycrystalline materials. The dataset encompasses a broad range of material types and compositions to promote the model's generalizability. It includes H_V data from systems that range from soft to superhard, and covers binary, ternary, and higher-order phases, along with solid solutions. A detailed analysis of the dataset is provided in the SI (Table S3), along with complete descriptions of structure preprocessing, including handling of partial and split occupancies, descriptor generation (elastic and structural), and model training workflows, such as GridSearchCV and leave-one-group-out cross-validation (LOGO-CV) (SI Section 1.2).

2.1.3 Oxidation temperature model. The supervised machine learning model was initially trained using XGBoost based on the same structural (17 features), compositional

descriptors (140 features), and MBTR descriptors as the hardness model. CIFs were downloaded for each compound in the training set and prepared for their respective compounds and structural descriptors were generated. A GridSearchCV facilitated the optimization of critical hyperparameters: the maximum depth of trees in the range of [3, 4, 5, 6, 7], the learning rate in a range of [0.01, 0.02, 0.03, 0.05, 0.07], column subsampling rate per tree of [0.6, 0.7, 0.8, 0.9], a minimum child weight in the range of [4, 5, 6, 7], the subsample ratio in each tree in the range of [0.6, 0.7, 0.8, 0.9], and gamma regularization of [0, 0.1, 0.01, 0.001, 0.0001]. Following the initial optimization, the feature set was refined with CV-RFE, ultimately retaining 34 of the most important features (see SI Table S6). A bagging strategy was incorporated with $n = 5$. A 10-fold cross-validation was performed across five random states, generating multiple out-of-sample predictions for each target value. The average of the cross-validated predictions across all folds and random states was used to derive the final predictions.[34] The final model yielded an R^2 value of 0.82 and a root mean squared error (RMSE) of 75 °C.

2.2 Synthesis

Polycrystalline samples were synthesized by arc melting the constituent elements under flowing argon on a water-chilled copper hearth. Raw starting materials were weighed in stoichiometric and near-stoichiometric ratios, with total masses ranging between 0.125 g and 0.25 g. The addition of excess boron, carbon, or silicon was periodically required to mitigate the formation of unwanted thermodynamically favored binary phases and promote phase purity of the more complex phases, as the excess compensates for any loss of the main group element through volatilization or spattering, for example, and shifts the equilibrium toward the target phase. The elements were loaded into a 6 mm die with a drop of hexanes to promote elemental binding and pressed into a pellet. The pellets were initially reacted with currents ranging from 10 A to 17 A. Depending on the constituent elements of the sample, the current was maintained throughout the synthesis or was incrementally increased up to 200 A. No noticeable deposition formed in the chamber during synthesis. The silicides were synthesized at lower currents, whereas boron-rich samples required higher currents. The samples were flipped at least once before re-melting the sample to promote sample homogeneity. The appearance of the as melted samples varied from dull, dark ingots to lustrous, faceted buttons. The mass of all samples was recorded pre- and post-synthesis to track potential mass loss. The mass loss was never greater than 5%; otherwise, the sample was remade. Select samples underwent an additional annealing step to promote solid–solid diffusion, ensuring the products are near thermodynamic equilibrium with respect to decomposition into competing phases. The annealing involved wrapping the ingots in tantalum foil, vacuum-sealing the samples in fused silica tubes, and annealing for one week to one month, at temperatures varying from 800 °C (silicon-containing samples) to 1000 °C (boron-containing samples) in Lindberg/Blue™ box furnaces.

2.3 Powder X-ray diffraction

Each arc-melted button was broken into two pieces. One half was pulverized into a fine-grained powder with a CerCo Diamonite™ mortar and pestle for X-ray diffraction analysis. The powder X-ray diffraction data were obtained using a PANalytical X'Pert Pro diffractometer, featuring Cu Kα radiation at a wavelength of 1.54183 Å from 5° 2θ to 90° 2θ. Scans collection times were up to 1 h to analyze product purity. The resulting diffractograms were then indexed against known phases in the International Center for Diffraction Data (ICDD) database using the HighScore software and manually indexed against patterns from PCD for potential phases in the sample. Accurate lattice parameters and confirmation of phase purity were achieved by performing Le Bail refinements using the EXPGUI[35] interface for the General Structure Analysis System (GSAS).[36]

2.4 Vickers microhardness

The other half of the crushed polycrystalline ingots were embedded in EpoxiCure 2 Epoxy Resin, and the surface was polished to achieve a smooth, mirror-like finish. Initial polishing with a diamond disc exposed the ingot surfaces, followed by sequential polishing with 800–1200 grit SiC plates in alternating orientations to minimize surface imperfections. Final polishing was performed manually using progressively finer diamond pastes until all visible striations were eliminated. This process helps to remove pits and voids on the surface that could interfere with accurate indentation measurements.

The polished ingots were subjected to Vickers microhardness testing to measure their hardness. The ingots were indented at different locations using the LECO AMH55, LM810AT Vickers microhardness indenter to ensure sample coverage. While the hardness values are expected to be consistent, slight variations may occur due to different underlying or secondary phases that might influence the material's resistance to deformation. Scanning electron microscopy (SEM) can help identify suitable areas of the target phase for indentation when dealing with multiphase samples or those featuring cracks or voids.

Each sample was indented at various loads to establish a load response curve. At least ten indentations were made at the 0.49 N (50 gf) applied load, and a minimum of five indentations were made at 0.98 N (100 gf), 1.96 N (200 gf), 2.94 N (300 gf), and 4.9 N (500 gf) applied loads. Indentations deviating from the standard square-based pyramid shape of the Vickers indenter tip were excluded from the hardness calculations to ensure accuracy and consistency. Moreover, brittle materials may develop sinkholes or cracks that emanate from the indent when subjected to higher loads. These responses made obtaining full load response curves in some samples challenging. The acceptable indents were measured both by eye and digitally using the LECO Cornerstone AMH55L software, and hardness values were calculated following eqn (1),[37]

$$H_V = 1.854\frac{F}{{D_{avg}}^2} \quad (1)$$

where F represents the applied force (in gram-force) and D_{avg}^2 denotes the average diagonal length of the Vickers indenter imprint (in millimeters).

2.5 Thermogravimetric analysis

The oxidation resistance of the samples was assessed by thermogravimetric analysis (TGA) using an EXSTAR 600 TG/DTA 6300 instrument. Phase purity was essential, as multiphase samples were excluded due to the difficulty of evaluating their complex oxidation kinetics. Approximately 10 mg to 15 mg of powder was taken from the same samples used for powder X-ray diffraction and loaded into an alumina crucible. The powders were heated from 25 °C to 870 °C at a rate of 20 °C min^{-1} under flowing purified air. The observed weight changes were plotted as a function of temperature to construct TGA curves. The first derivative peak temperature (T_p), representing the point of maximum weight change rate, was used to determine oxidation resistance. T_p was obtained from the first derivative of the TGA curve, excluding the initial and final temperature regions. There are multiple ways that oxidation temperatures could be considered, such as the onset oxidation temperature (T_o), which is often defined as a 5% increase in the baseline; however, the first derivative value was found to be the most consistent between the in-house measurements and the literature measurements. The alumina crucibles were stored in a drying oven at 175 °C to reduce moisture absorption.

Generally, metal powders exhibit weight gain due to oxidation. However, in some instances, like with Mo-containing samples, weight loss was observed due to the volatilization of the product during oxidation. Changes in the powders' color and consistency were noted as early indicators of oxidation. Samples where obvious oxidation temperatures (T_p values) could not be obtained were excluded from subsequent analysis.

Caution! The oxidation of elements like chromium, boron, molybdenum, and osmium can produce hazardous oxides requiring proper precautions: chromium oxides (CrO_3, Cr_2O_3, CrO_2) and osmium tetroxide (OsO_4) are highly toxic, potent oxidizers, and volatile, with risks of severe irritation to eyes, skin, and respiratory systems. Boron oxide (B_2O_3), which is a strong desiccant, and molybdenum trioxide (MoO_3) can cause eye, skin, and respiratory tract irritation. They require handling in a fume hood with appropriate PPE, including gloves and eye protection. In the event of exposure, immediate medical attention is necessary. Follow all institutional safety protocols and OSHA guidelines.

3. Results and discussion

This study develops supervised machine learning models based on XGBoost to predict Vickers microhardness and the T_p oxidation temperature using compositional and structural descriptors. The approach begins by training models to predict bulk and shear moduli, which are physically grounded proxies for mechanical response.[11] These predicted moduli are then incorporated as input features in the final hardness and oxidation models, enabling the capture of complex, underlying relationships between structure, chemistry, and target properties.

3.1 Machine learning prediction of elastic moduli

Materials with high resistance to volumetric compression and shear deformation exhibit high bulk and shear moduli, which are key indicators of mechanical robustness. These elastic properties are characteristic of superhard materials such as diamond and serve as critical design targets for developing next-generation hard materials. Fortunately, Density Functional Perturbation Theory (DFPT) provides a reliable framework for calculating the effects of elastic strain, and DFPT-derived moduli for a wide range of inorganic compounds are available through the Materials Project database. By leveraging this information, machine learning models can be trained to predict elastic behavior and enable the use of this information as a descriptor in the subsequent prediction of mechanical properties.

Building on our group's prior work,[11] which successfully screened for superhard materials using machine learning models trained on DFT-derived elastic moduli, we redeveloped two models to predict bulk and shear moduli using values sourced from the Materials Project. The training set consisted of 7148 curated binary and ternary inorganic compounds, prepared following the workflow described in the Experimental section. Both models employed a bagged extreme gradient boosting ensemble with 10 estimators and final feature sets comprising 71 and 144 descriptors for bulk and shear models, respectively.

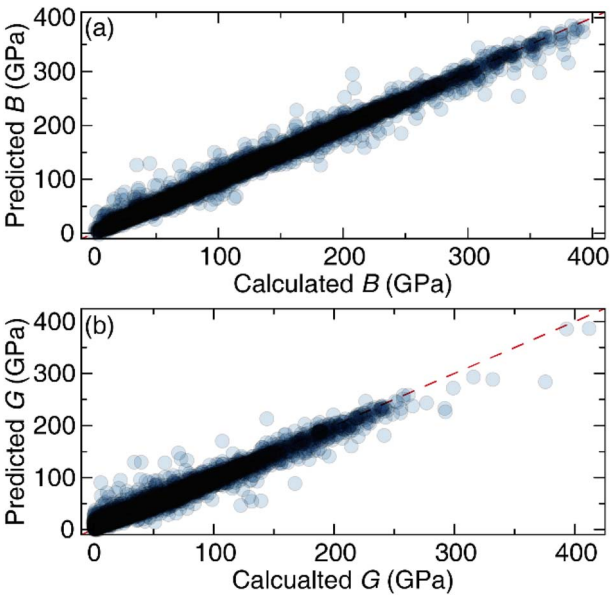

Fig. 1 Predicted *versus* DFT-calculated elastic moduli for the (a) bulk modulus (B) and (b) shear modulus (G) using the extreme gradient boosting model trained on 7148 inorganic compounds. DFT-calculated values were obtained from the Materials Project database. Model performance was evaluated using 10-fold cross-validation. The red dashed line represents the ideal 1 : 1 parity line.

As shown in Fig. 1a and b, both models exhibit strong agreement with DFT reference values, achieving R^2 scores of 0.97 for the bulk modulus model and 0.85 for the shear model with corresponding mean absolute errors (MAEs) of 7.47 GPa and 9.9 GPa, respectively. Approximately 22% of bulk predictions and ~11% of shear predictions fall within 1 GPa of the reference values. High prediction accuracy was observed for intermetallics such as $ZrNi_2P_2$ and $AlPt_2$, as well as chalcogenides like $CsCuSe_4$ and $NaTbSe_2$. Notably, the shear model performed especially well for alkali and alkaline earth compounds, potentially due to their relatively simple ionic bonding environments. The most significant prediction errors were observed in nitrides, borides, and select transition metal compounds. These systems often feature rigid crystal structures or pronounced bonding anisotropy, which may not be fully captured by the current descriptor set. While absolute errors exceeding 90 GPa were rare, such discrepancies underscore the need for improved feature representations that more explicitly account for bonding character, crystal symmetry, and elastic anisotropy.

3.2 Predicting Vickers microhardness

Load-dependent Vickers microhardness has previously been predicted with high accuracy using a composition-based machine learning model.[9] However, a significant limitation of this model, which relied on composition-only descriptors, is the inability to distinguish between polymorphs and allotropes. Materials that share identical chemical compositions can still exhibit vastly different hardness values depending on the structure, with the obvious example of graphite's layers held together by weak van der Waals forces, resulting in a soft and easily cleavable structure compared to diamond's three-dimensional covalent network.[38,39] A new model was therefore developed here to address this limitation, expanding beyond the limited composition-only model by using a descriptor set that explicitly encodes crystal structure information through the Many-Body Tensor Representation (MBTR). MBTR captures structural information through geometry-based functions, where the $k = 1$ term encodes atomic identities, while the $k = 2$ term captures pairwise interatomic distances. The structure-aware model also includes the predicted bulk and shear moduli and derived quantities like Poisson's ratio as the mechanical property descriptors.

An analysis of elemental frequency, hardness distribution, and applied loads for the training dataset of 1225 compounds revealed that over half of the dataset contains boron. Most compounds exhibit Vickers hardness values within or near the 10–15 GPa range, while only 20 unique materials meet the superhard threshold (≥40 GPa). The dataset is also skewed toward low-load measurements, with 400 compounds tested at 0.49 N. This distribution reflects the available data in the literature and highlights the frequent challenge of data imbalance when applying data-driven methods to materials research.

The model was trained using extreme gradient boosting and optimized *via* hyperparameter tuning. Cross-validated recursive feature elimination reduced the feature set to 11 key structural and physical features with the LOGO-CV strategy to ensure generalization and prevent data leakage. Three bagging estimators were employed, grouping data by composition while allowing variation in applied load. This ensured the evaluation of entirely unseen chemical systems. The final model, shown in Fig. 2, achieved strong predictive performance, with an ensemble-averaged R^2 of 0.83 and an MAE of 3.0 GPa. It effectively captured load-dependent hardness across diverse systems, including simple binaries, solid solutions, and complex boron-rich phases such as $YB_{41.2}Si_{1.42}$. High accuracy was observed for ternary intermetallic borides such as $AlLiB_{14}$ and $AlMgB_{14}$, consistent with their dense bonding networks and well-defined structure–property relationships. In contrast, the structure-aware model overestimated hardness for soft, layered compounds like graphite and h-BN, and significantly underestimates superhard materials (H_V > 60 GPa) such as diamond and c-BN. This reflects challenges in capturing extremes in hardness, particularly when the crystal structures of such materials are not well represented in the training data.

For completeness, a model that combined the MBTR-based features described here, as well as the complete compositional features used in the original model, was also evaluated. The resulting overall statistical performance was comparable to the MBTR-based model; however, closer examination showed this model exhibited reduced accuracy for carbon and boron nitride allotropes. This suggests that capturing polymorph- and allotrope-specific behavior remains challenging even with structure and composition descriptors both included. Given the greater complexity of this joint feature (MBTR and composition) model and the potential risk of overfitting from a substantial number of features on this dataset that is rather limited in size,

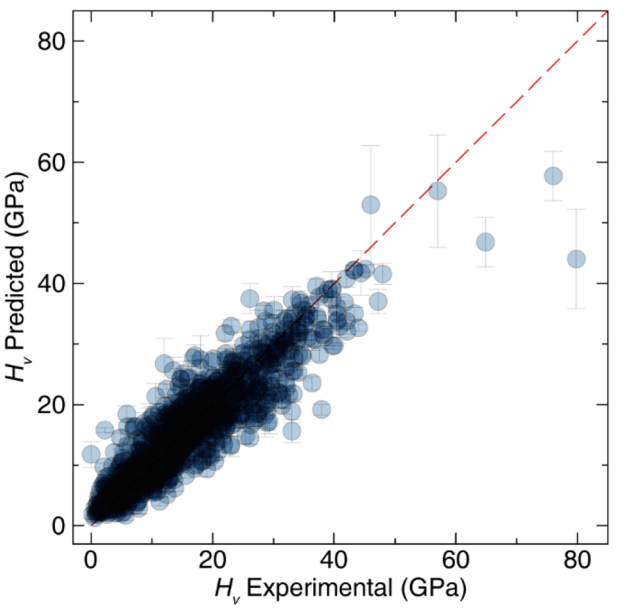

Fig. 2 Experimentally measured Vickers microhardness ($H_{V,exp}$) plotted against the predicted values ($H_{V,pred}$) from the XGBoost model for 1225 inorganic compounds. Error bars represent the standard deviation across three bagging estimators. The red dashed line indicates the ideal fit.

the MBTR-based only model was selected for subsequent hardness predictions.

3.3 Predicting oxidation temperature

3.3.1 Model performance. The accuracy and reliability of machine learning models are fundamentally tied to the quality, consistency, and diversity of the training data. Building a cohesive collection of oxidation temperatures has not been done previously. As a result, significant effort was dedicated to constructing a robust dataset by combining T_p oxidation temperatures of compounds synthesized in-house with carefully curated literature values. Given that parameters such as ramp rate, impurity phases, synthesis conditions, particle size, and sample morphology (*e.g.*, single crystal *vs.* polycrystalline) can significantly influence oxidation behavior, careful consideration was given to data selection. We, therefore, limited literature values to those reported by H. E. N. Stone,[40–45] whose experimental methods are well-documented and reliable to ensure consistency and reproducibility. Additional in-house measurements were performed using procedures that closely matched Stone's methods, enabling a high-quality dataset tailored for model training. In total, the dataset included the oxidation temperature of 348 compounds.[40–45] Of these, 71 that were synthesized in-house and evaluated by thermogravimetric analysis (TGA) (see SI Table S5). This dataset covers a wide range of inorganic material classes, including borides, silicides, carbides, and aluminides. It contains mostly binary compounds, but also includes select ternaries, quaternaries, and solid solutions to support model generalizability.

There are multiple ways to define the oxidation temperature. Here we determined the oxidation temperatures (T_p) based on the first derivative peaks ($d\Delta m/dT$) of in-house thermogravimetric analysis (TGA) curves. The full set of experimental TGA curves is shown in Fig. 3a, illustrating the diversity of oxidation behavior. Some compounds, like ReB_2, showed continuous mass loss upon heating. MoB exhibited initial mass gain followed by rapid loss above 700 °C, likely due to volatilization of molybdenum oxides. In contrast, YB_{66} showed consistent mass gain throughout the experiment.

Importantly, compounds with similar $d\Delta m/dT$ values but differing mechanisms, such as mass loss *versus* mass gain, present a challenge for model training. Any phases exhibiting significant volatilization were excluded from the training dataset to mitigate issues related to estimating T_p. Additionally, only two WB polymorphs (MoB-type and TlI-type) were included, in contrast to the broader polymorph set used in the hardness model. The polymorphs showed similar T_p values of 550 °C and 500 °C, respectively, suggesting that phase differences may play a limited role in T_p for these materials. The complete dataset is detailed in the SI Table S5.

Several modeling strategies were evaluated to find the optimal performance, such as a simple decision tree, as well as random forest, LightGBM and CatBoost. Models incorporating dataset separation by source and a weighting factor were also explored. However, many of these approaches did not yield models capable of quantitative T_p prediction. XGBoost was ultimately selected due to its strong performance on small datasets.[25,33] The final XGBoost model was trained on a reduced set of 34 descriptors encompassing compositional, structural, and elastic features, including MBTR terms that encode local atomic environments, selected using recursive feature elimination (CV-RFE) as detailed in the Experimental section. Hyperparameters were optimized using grid search, and five-fold cross-validation across multiple random states was applied to improve robustness. Bagging with five estimators further reduced the variance due to data partitioning.

The parity plot for model training using the 348 compounds were generated using the optimized XGBoost model. As shown in Fig. 3b, the predicted oxidation temperatures ($T_{p,pred}$) align closely with experimental values, with the error bars providing further clarity on the uncertainty of the predictions from five bagging estimators. The model achieved an aggregated $R^2 = 0.82$ and a root-mean-square error of ~75 °C. Prediction accuracy was highest between 400 and 800 °C, corresponding to the most populated region of the dataset.

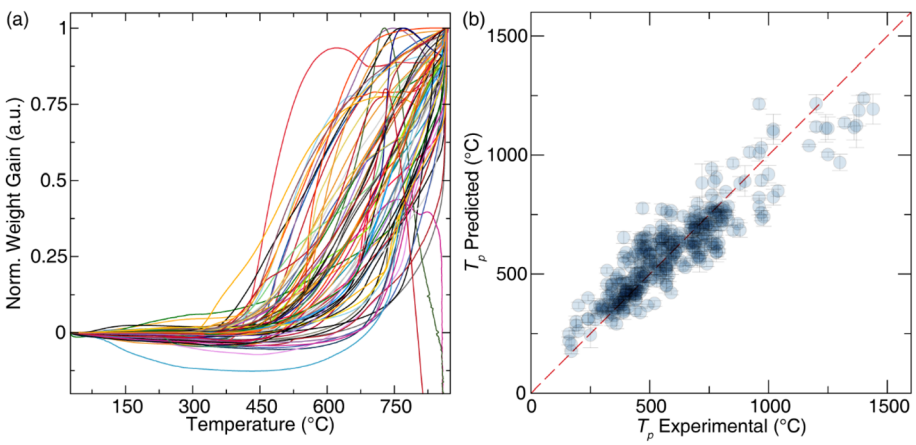

Fig. 3 (a) Thermogravimetric analysis (TGA) curves for the training dataset, measured in air up to 870 °C, showing normalized weight gain as a function of temperature. (b) Predicted oxidation temperatures (T_p) from the optimized machine learning model plotted against experimentally measured values. The dashed red line denotes a 1 : 1 correlation. Error bars correspond to the standard deviation of the bagging estimators.

As observed in the structure-based hardness model, systematic deviations occurred at the extremes, with low T_p values tending to be overpredicted and high T_p values often underpredicted. This trend likely results from data imbalance and limited representation of compounds exhibiting extreme oxidation behavior. Despite these challenges, the model showed excellent performance for several families. For instance, Zn-containing compounds such as $TiZn_3$ and $GdZn_2$ were predicted within 2 °C of experimental values. Ternary and higher-order borides, including Y_2OsB_6, (TaHfZr)Ru_5B_2, and $LaIr_2B_2$-C, were also predicted with high accuracy. This is likely due to the dataset's boron-rich composition which accounts for approximately 25% of the samples. Aluminum-containing materials posed greater difficulty. Some, like $AlNd_3$ and Al_4Ir, were predicted with <0.5 °C deviation. Others, such Al_2Au and Al_3Tb, had errors exceeding 300 °C. Although Al-containing compounds comprise more than 25% of the training dataset, they disproportionately contributed to the total error. This is likely due to aluminum's complex oxidation behavior, which may involve passivating Al_2O_3 layer formation in some compositions but not others; this phenomena not captured by the current descriptors. Nevertheless, the model's performance is clearly sufficient form making T_p predictions of unknown compounds.

3.3.2 Experimental validation of oxidation temperature. Rigorous model performance was validated against a series of unseen compounds spanning diverse chemistries, including binary and ternary systems. This in-house dataset served as an independent benchmark, enabling direct assessment of predictive accuracy under strictly controlled experimental conditions. Each compound was synthesized using direct reaction of the elements (seal tube reactions or arc melting) and characterized through Le Bail refinements of the powder X-ray diffractograms (Fig. S1–S5). Most of the compounds are single phase, with only minor secondary phases occasionally indexed. The oxidation temperatures were experimentally determined by TGA (Fig. 4a) and compared to predictions from the ensemble model. As shown in Fig. 4b, the validation set shows strong agreement with an R^2 of 0.76 and an RMSE of ~72.8 °C, closely matching the training performance and confirming the model's generalizability.

Table 1 provides several boron- and silicon-containing binaries, such as LaB_6, Er_5Si_3, and the ternary compound ScRuGe were predicted with high accuracy. The lone Al-containing compound in the validation set continued to challenge the model, likely due to surface effects. YAg, a low T_p material, was also overpredicted. Nonetheless, most validation compounds oxidized between 400 and 800 °C, and predictions in this range clustered tightly around the 1 : 1 line. Overall, these results demonstrate that the model effectively predicts oxidation temperatures for a broad range of inorganic materials, while also highlighting the need for better surface- and kinetic-aware descriptors to improve accuracy at the extremes.

3.4 Screening ternary compounds for multifunctional candidates

Once the two primary machine learning models (hardness and oxidation) were optimized, they were deployed to identify the H_V and T_p of multifunctional materials with robust mechanical response and thermal stability. Specifically, this study focuses on the underexplored phase spaces of pseudo-binary and ternary compounds. This restriction is intentional, as these systems are well represented and structurally reliable within the Materials Project, making them an appropriate space to demonstrate the framework. Future work will extend the approach to higher-order systems, which will require additional validation of structural data and model performance. The structures were obtained from the Materials Project to enable high-throughput screening. The screening strategy prioritized light elements such as B, C, and Si due to their roles in forming hard materials[46,47] and promoting oxidation resistance, primarily through the formation of protective SiO_2 layers in silicon-containing compounds.[48] Rare earth elements were selected for their contribution to oxidation resistance *via* the

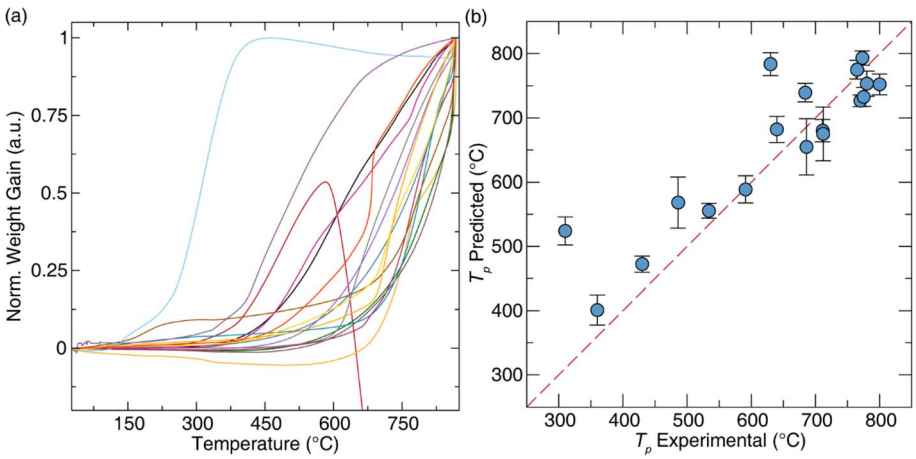

Fig. 4 (a) Thermogravimetric analysis curves for the validation dataset, measured in air up to 870 °C, showing normalized weight gain profiles. (b) Correlation of experimental T_p oxidation temperature with predictions for the optimized machine learning model. The dashed red line denotes a 1 : 1 correlation. Error bars indicate the standard deviation across bagged estimators.

Table 1 Experimental T_p for the validation dataset compared with aggregated model predictions. Reported uncertainties correspond to the standard deviation across bagged estimators

Formula	Actual T_p	Pred. T_p (Agg.)	Pred. Std.
AlMnGe	630	783.6	17.6
DyB_4	773	793.1	10.9
Er_3Ru	430	472.2	12.6
Er_5Si_3	534	555.5	11.6
Hf_9Re_4B	486	568.3	39.8
$LaAu_2$	360	401.0	23.4
LaB_6	765	775.0	14.5
NdB_6	800	752.3	16.3
ScRuGe	591	588.8	21.0
$Sc_2Cr_3Si_4$	711	680.1	17.5
TaB_2	640	681.9	20.2
Ta_2Si	686	654.9	43.9
YAg	310	524.0	21.9
YCr_2Si_2	712	674.9	41.8
Y_3Si_5	684	739.5	14.5
ZrB_2	770	726.7	9.1
$ZrSi_2$	775	732.9	14.8
Zr_5Si_4	780	753.5	19.7

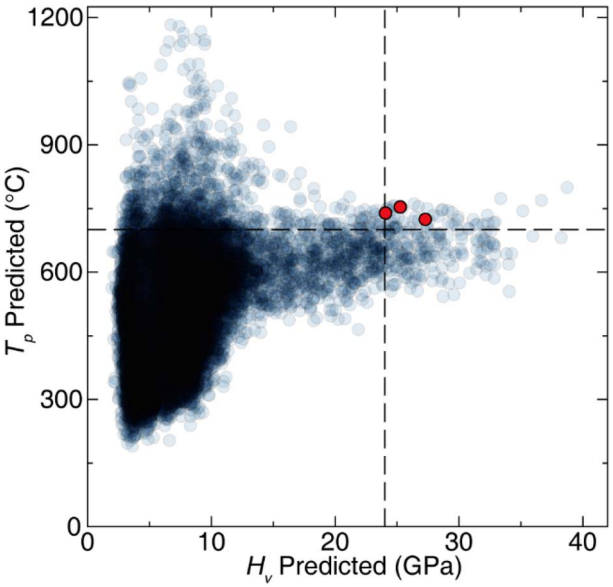

Fig. 5 Predicted Vickers microhardness (H_V) plotted against predicted oxidation temperature (T_p) for 15 247 pseudo-binary and ternary inorganic compounds extracted from the Materials Project. Dashed lines at 24 GPa and 700 °C represent thresholds for hardness and thermal stability, respectively. Three target compounds selected for future experimental validation are highlighted in red.

reactive element effect (REE),[49,50] where interfacial segregation at the oxide–metal interface enhances scale cohesion, suppresses void formation, and impedes oxygen penetration. These mechanisms collectively promote long-term stability in high-temperature environments. Transition metals were selected based on the well-documented hardness of binary and higher-order borides.[51] Alkali and alkaline earth elements were excluded because of their air sensitivity, reactivity, and volatility during synthesis. Radioactive and otherwise inaccessible elements were also omitted to maintain experimental synthesis feasibility. This filtering strategy integrates functionality, literature precedent, and practical constraints to focus the search on promising candidates for applications in extreme environments.

The final screening dataset comprised 15 247 compounds. The two independent models (Vickers microhardness and oxidation temperature) were constructed using features following the same workflow developed during model training. The resulting predictions for all compounds were then analyzed using the sorting diagram plotted in Fig. 5, which shows the predicted hardness values plotted against predicted oxidation temperatures.

Several extreme cases illustrate the predictive strength of these models. For instance, $REAlB_{14}$-type compounds,[52] where RE = Yb, Tb, or Ho, exhibit predicted microhardness values between 36(1) GPa and 38(1) GPa. These structures feature B_{12} icosahedra, commonly found in hard and superhard materials, making them particularly attractive for applications where resistance to plastic deformation is essential.[53–55] Five compounds in the Al–Ni–Pt ternary system show predicted oxidation temperatures above 1000 °C, suggesting excellent thermal stability. The formation of a passivating Al_2O_3 surface layer likely drives this behavior, as it is a well-established oxidation resistance mechanism in Al-containing compounds.[56]

Beyond these most promising phases, the screening focused on compounds with predicted microhardness values exceeding 24 GPa and oxidation temperatures above 700 °C. These thresholds effectively narrowed the set of candidates for further synthesis and characterization. Most of the selected compounds were boron-rich systems, consisting of complex rare earth transition metal borides with parent structures such as Er_4NiB_{13},[57] Th_2NiB_{10},[58] $YCrB_4$,[59] and Y_2ReB_6 [60] and pseudo-binary transition metal dodecaborides. This outcome reflects chemical intuition, as many of these structure types exhibit high hardness and allow further tuning through solid solution effects.[61] Indeed, our experimental results confirm that $YTMB_4$ compounds (TM = Ru, Os) with the $YCrB_4$-type structure exhibit both high oxidation temperatures and significant hardness, validating the model's prediction of analogous materials as multifunctional candidates. The $ErNiB_4$-type structure is stoichiometrically analogous to the $YCrB_4$-type structure but adopts a distinct, non-isostructural framework, making it a compelling target for further investigation. Notably, structures such as Er_4NiB_{13}-type and Th_2NiB_{10}-type were not included in the training dataset, making them ideal targets for experimental validation.

Interestingly, the Th_2NiB_{10}-type structure resembles the LaB_6 framework, where a nickel atom occupies the 2*a* Wyckoff site instead of two boron atoms linking adjacent octahedra.[62] Such structural analogies may contribute to its high predicted oxidation resistance, consistent with the behavior of LaB_6 observed in the validation set of the oxidation model. Combining rare earth elements and high boron content creates unique bonding motifs that mirror known hard and thermally

stable materials. Based on these insights, compounds from the Gd–Ni–B system, namely Gd_4NiB_{13}, Gd_2NiB_{10}, and $GdNiB_4$, are prime candidates for synthesis and validation. As reported in the literature, researchers have synthesized all these compounds by arc melting.

4. Conclusion

This work demonstrates that integrating structural, chemical, and mechanically informed descriptors within a targeted machine learning framework enables the accurate identification of materials that simultaneously exhibit high hardness and oxidation resistance, which are key requirements for structural materials operating in high-temperature environments. The models maintain robust performance across a chemically diverse space by leveraging composition, crystal structure, and physically grounded properties such as predicted bulk and shear moduli. Applying the resulting machine learning framework to predict the response of over 15 000 compounds revealed that rare earth transition metal borides are especially promising candidates, underscoring the power of model-driven screening to accelerate experimental discovery. Although this screening focused on pseudo-binary and ternary systems, the framework is general and can be extended to higher-order chemistries following appropriate validation. Looking forward, extending the approach to incorporate complete oxidation pathways through raw TGA data, *in situ* phase evolution, and surface kinetics could yield richer descriptors that move beyond thermodynamic thresholds toward a mechanistic understanding of oxidation resistance, paving the way for the design of truly resilient materials.

Author contributions

Roy Arrieta and Amit Kumar provided compounds for TGA and hardness measurements. Compounds were synthesized by Arman Karimaghaei, Gonzalo Cuervo, Matt Flores, Peter Zhu, Sally Hoang, and Jacob Hickey. Arman Karimaghaei, Matt Flores, Gonzalo Cuervo, and Jacob Hickey performed the TGA experiments, while hardness measurements were conducted by Arman Karimaghaei, Matt Flores, Gonzalo Cuervo, Peter Zhu, and Jacob Hickey. Jacob Hickey and Arman Karimaghaei developed the computational code, with Jacob Hickey leading coding. Jakoah Brgoch and Jacob HIckey lead the manuscript writing and editing.

Conflicts of interest

There are no conflicts to declare.

Data availability

Data are available including the optimized models, training data, and prediction sets are provided in the open-source GitHub repository at **https://github.com/BrgochGroup**.

Supplementary information is available. See DOI: **https://doi.org/10.1039/d5sc05800g**.

Acknowledgements

The authors thank the Texas Center for Superconductivity at the University of Houston (TcSUH) and the Welch Foundation (E-2181) for providing financial support. The authors gratefully acknowledge Dr Shiv Halasyamani and his group for support performing the TGA measurements.

References

1 E. Wuchina, E. Opila, M. Opeka, B. Fahrenholtz and I. Talmy, UHTCs: Ultra-High Temperature Ceramic Materials for Extreme Environment Applications, *Electrochem. Soc. Interface*, 2007, **16**, 30, DOI: **10.1149/2.F04074IF**.

2 P. Sengupta and I. Manna, Advanced High-Temperature Structural Materials for Aerospace and Power Sectors: A Critical Review, *Trans. Indian Inst. Met.*, 2019, **72**, 2043–2059, DOI: **10.1007/s12666-019-01598-z**.

3 B. Gorr, S. Schellert, F. Müller, H.-J. Christ, A. Kauffmann and M. Heilmaier, Current Status of Research on the Oxidation Behavior of Refractory High Entropy Alloys, *Adv. Eng. Mater.*, 2021, **23**, 1–14, DOI: **10.1002/adem.202001047**.

4 D. Ni, Y. Cheng, J. Zhang, J.-X. Liu, J. Zou, B. Chen, H. Wu, H. Li, S. Dong, J. Han, X. Zhang, Q. Fu and G.-J. Zhang, Advances in Ultra-High Temperature Ceramics, Composites, and Coatings, *J. Adv. Ceram.*, 2021, **11**, 1–56, DOI: **10.1007/s40145-021-0550-6**.

5 J. R. Salvador, C. Malliakas, J. R. Gour and M. G. Kanatzidis, $RE_5Co_4Si_{14}$ (RE = Ho, Er, Tm, Yb): Silicides Grown from Ga Flux Showing Exceptional Resistance to Chemical and Thermal Attack, *Chem. Mater.*, 2005, **17**, 1636–1645, DOI: **10.1021/cm047959w**.

6 B. Sieve, D. L. Gray, R. Henning, T. Bakas, A. J. Schultz and M. G. Kanatzidis, Al Flux Synthesis of the Oxidation-Resistant Quaternary Phase $REFe_4Al_9Si_6$ (RE = Tb, Er), *Chem. Mater.*, 2008, **20**, 6107–6115, DOI: **10.1021/cm801554d**.

7 A. R. Oganov, C. J. Pickard, Q. Zhu and R. J. Needs, Structure Prediction Drives Materials Discovery, *Nat. Rev. Mater.*, 2019, **4**, 331–348, DOI: **10.1038/s41578-019-0101-8**.

8 Z. Zhang, A. Mansouri Tehrani, A. O. Oliynyk, B. Day and J. Brgoch, Finding the Next Superhard Material through Ensemble Learning, *Adv. Mater.*, 2021, **33**, 2005112, DOI: **10.1002/adma.202005112**.

9 J. C. Hickey and J. Brgoch, The Limits of Proxy-Guided Superhard Materials Screening, *Chem. Mater.*, 2022, **34**, 10003–10010, DOI: **10.1021/acs.chemmater.2c02390**.

10 P. Avery, X. Wang, C. Oses, E. Gossett, D. M. Proserpio, C. Toher, S. Curtarolo and E. Zurek, Predicting Superhard Materials via a Machine Learning Informed Evolutionary Structure Search, *npj Comput. Mater.*, 2019, **5**, 89, DOI: **10.1038/s41524-019-0226-8**.

11 A. M. Tehrani, A. O. Oliynyk, M. Parry, Z. Rizvi, S. Couper, F. Lin, L. Miyagi, T. D. Sparks and J. Brgoch, Machine Learning Directed Search for Ultraincompressible, Superhard Materials, *J. Am. Chem. Soc.*, 2018, **140**, 9844–9853, DOI: **10.1021/jacs.8b02717**.

12 R. Jin, X. Yuan and E. Gao, Atomic Stiffness for Bulk Modulus Prediction and High-Throughput Screening of Ultraincompressible Crystals, *Nat. Commun.*, 2023, **14**, 4258, DOI: **10.1038/s41467-023-39826-2**.

13 H. Khakurel, M. F. N. Taufique, A. Roy, G. Balasubramanian, G. Ouyang, J. Cui, D. D. Johnson and R. Devanathan, Machine Learning Assisted Prediction of the Young's Modulus of Compositionally Complex Alloys, *Sci. Rep.*, 2021, **11**, 17149, DOI: **10.1038/s41598-021-96507-0**.

14 M. Kandavalli, A. Agarwal, A. Poonia, M. Kishor and K. P. R. Ayyagari, Design of High Bulk Moduli High Entropy Alloys using Machine Learning, *Sci. Rep.*, 2023, **13**, 20504, DOI: **10.1038/s41598-023-47181-x**.

15 S. Biswas, D. Fernandez Castellanos and M. Zaiser, Prediction of Creep Failure Time using Machine Learning, *Sci. Rep.*, 2020, **10**, 16910, DOI: **10.1038/s41598-020-72969-6**.

16 A. Rovinelli, M. D. Sangid, H. Proudhon and W. Ludwig, Using Machine Learning and a Data-Driven Approach to Identify the Small Fatigue Crack Driving Force in Polycrystalline Materials, *npj Comput. Mater.*, 2018, **4**, 35, DOI: **10.1038/s41524-018-0094-7**.

17 H. Wang, B. Li, J. Gong and F.-Z. Xuan, Machine Learning-Based Fatigue Life Prediction of Metal Materials: Perspectives of Physics-Informed and Data-Driven Hybrid Methods, *Eng. Fract. Mech.*, 2023, **284**, 109242, DOI: **10.1016/j.engfracmech.2023.109242**.

18 H. Salmenjoki, M. J. Alava and L. Laurson, Machine Learning Plastic Deformation of Crystals, *Nat. Commun.*, 2018, **9**, 5307, DOI: **10.1038/s41467-018-07737-2**.

19 T. D. Sparks, S. K. Kauwe, M. E. Parry, A. M. Tehrani and J. Brgoch, Machine Learning for Structural Materials, *Annu. Rev. Mater. Res.*, 2020, **50**, 27–48, DOI: **10.1146/annurev-matsci-110519-094700**.

20 J. Schmidt, M. R. G. Marques, S. Botti and M. A. L. Marques, Recent Advances and Applications of Machine Learning in Solid-State Materials Science, *npj Comput. Mater.*, 2019, **5**, 83, DOI: **10.1038/s41524-019-0221-0**.

21 R. Chawuthai, T. Promchan, J. Rojsanga, S. Chandra-ambhorn, T. Nilsonthi, P. Wongpromrat, E. Bumrungthaichaichan and A. Anantpinijwatna, Novel Method for Predicting the Cracks of Oxide Scales During High Temperature Oxidation of Metals and Alloys by Using Machine Learning, *Sci. Rep.*, 2025, **15**, 7758, DOI: **10.1038/s41598-025-91449-3**.

22 X. Jia and H. Li, Machine Learning Enabled Exploration of Multicomponent Metal Oxides for Catalyzing Oxygen Reduction in Alkaline Media, *J. Mater. Chem. A*, 2024, **12**, 12487–12500, DOI: **10.1039/D4TA01884B**.

23 X. Tan, W. Trehern, A. Sundar, Y. Wang, S. San, T. Lu, F. Zhou, T. Sun, Y. Zhang, Y. Wen, Z. Liu, M. Gao and S. Hu, Machine Learning and High-Throughput Computational Guided Development of High Temperature Oxidation-Resisting Ni-Co-Cr-Al-Fe Based High-Entropy Alloys, *npj Comput. Mater.*, 2025, **11**, 93, DOI: **10.1038/s41524-025-01568-8**.

24 C. Li, K. Xu, M. Lou, L. Wang and K. Chang, Machine Learning-Enabled Prediction of High-Temperature Oxidation Resistance for Ni-based Alloys, *Corros. Sci.*, 2024, **234**, 112152, DOI: **10.1016/j.corsci.2024.112152**.

25 T. Chen and C. Guestrin, XGBoost: A Scalable Tree Boosting System, in *Proceedings of the 22nd ACM SIGKDD International Conference on Knowledge Discovery and Data Mining*, 2016, pp. 785–794, DOI: **10.1145/2939672.2939785**.

26 A. Jain, S. P. Ong, G. Hautier, W. Chen, W. D. Richards, S. Dacek, S. Cholia, D. Gunter, D. Skinner, G. Ceder and K. A. Persson, Commentary: The Materials Project: A Materials Genome Approach to Accelerating Materials Innovation, *APL Mater.*, 2013, **1**, 011002, DOI: **10.1063/1.4812323**.

27 Y. Le Page and P. Saxe, Symmetry-General Least-Squares Extraction of Elastic Data for Strained Materials from *ab initio* Calculations of Stress, *Phys. Rev. B: Condens. Matter Mater. Phys.*, 2002, **65**, 104104, DOI: **10.1103/PhysRevB.65.104104**.

28 G. Kresse and J. Furthmüller, Efficient Iterative Schemes for *ab initio* Total-Energy Calculations Using a Plane-Wave Basis Set, *Phys. Rev. B: Condens. Matter Mater. Phys.*, 1996, **54**, 11169–11186, DOI: **10.1103/PhysRevB.54.11169**.

29 J. P. Perdew, K. Burke and M. Ernzerhof, Generalized Gradient Approximation Made Simple, *Phys. Rev. Lett.*, 1996, **77**, 3865–3868, DOI: **10.1103/PhysRevLett.77.3865**.

30 V. I. Anisimov, J. Zaanen and O. K. Andersen, Band Theory and Mott Insulators: Hubbard *U* Instead of Stoner *I*, *Phys. Rev. B: Condens. Matter Mater. Phys.*, 1991, **44**, 943–954, DOI: **10.1103/PhysRevB.44.943**.

31 R. Hill, The Elastic Behaviour of a Crystalline Aggregate, *Proc. Phys. Soc., A*, 1952, **65**, 349, DOI: **10.1088/0370-1298/65/5/307**.

32 C. Zhang and Y. Ma, *Ensemble Machine Learning Methods and Applications*, Springer, 2012.

33 J. Brownlee, *XGBoost with Python: Gradient Boosted Trees with XGBoost and scikit-learn*, Machine Learning Mastery, 2016.

34 L. Breiman, Bagging Predictors, *Mach. Learn.*, 1996, **24**, 123–140, DOI: **10.1007/BF00058655**.

35 B. H. Toby, EXPGUI, A Graphical User Interface for GSAS, *J. Appl. Cryst.*, 2001, **34**, 210–213, DOI: **10.1107/S0021889801002242**.

36 B. H. Toby and R. B. Von Dreele, GSAS-II: The Genesis of a Modern Open-Source All Purpose Crystallography Software Package, *J. Appl. Cryst.*, 2013, **46**, 544–549, DOI: **10.1107/S0021889813003531**.

37 J. J. Gilman, *Chemistry and Physics of Mechanical Hardness*, John Wiley & Sons, Inc., 2009.

38 I. Iswandi, J. Sahari and A. B. Sulong, Effects of Different Particles Sizes of Graphite on the Engineering Properties of Graphites/Polypropylene Composites on Injection Molding Aplication, *Key Eng. Mater.*, 2011, **471–472**, 109–114, DOI: **10.4028/www.scientific.net/KEM.471-472.109**.

39 S. Dub, P. Lytvyn, V. Strelchuk, A. Nikolenko, Y. Stubrov, I. Petrusha, T. Taniguchi and S. Ivakhnenko, Vickers Hardness of Diamond and cBN Single Crystals: AFM Approach, *Crystals*, 2017, **7**, 369, DOI: **10.3390/cryst7120369**.

40 H. E. N. Stone, The Oxidation Resistance and Hardness of Some Intermetallic Compounds, *J. Mater. Sci.*, 1974, **9**, 607–613, DOI: **10.1007/BF00551880**.
41 H. E. N. Stone, The Oxidation Resistance, Hardness and Constitution of Metallic Aluminides, *J. Mater. Sci.*, 1975, **10**, 923–934, DOI: **10.1007/BF00823208**.
42 H. E. N. Stone, The Oxidation Resistance, Hardness and Constitution of Some Intermetallic Compounds Containing Zinc, *J. Mater. Sci.*, 1975, **10**, 923–924, DOI: **10.1007/BF02396646**.
43 H. E. N. Stone, The Oxidation Resistance and Constitution of Compounds of Groups IIIA and IVA with d-Transition Elements, *J. Mater. Sci.*, 1989, **24**, 633–640, DOI: **10.1007/BF01107454**.
44 H. E. N. Stone, The Oxidation Resistance and Constitution of Y_9Co_7 and Nearly-Related Compounds, *J. Mater. Sci.*, 1987, **22**, 1749–1752, DOI: **10.1007/BF01132402**.
45 H. E. N. Stone, The Thermal Oxidation of some Cu-Y-Ba Alloys, *J. Mater. Sci. Lett.*, 1989, **8**, 753–754, DOI: **10.1007/BF01730126**.
46 S. Vepřek, The Search for Novel, Superhard Materials, *J. Vac. Sci. Technol., A*, 1999, **17**, 2401–2420, DOI: **10.1116/1.581977**.
47 R. B. Kaner, J. J. Gilman and S. H. Tolbert, Designing Superhard Materials, *Science*, 2005, **308**, 1268–1269, DOI: **10.1126/science.1109830**.
48 R. Mitra, Mechanical Behaviour and Oxidation Resistance of Structural Silicides, *Int. Mater. Rev.*, 2006, **51**, 13–64, DOI: **10.1179/174328006X79454**.
49 J. Stringer, The Reactive Element Effect in High-Temperature Corrosion, *Mater. Sci. Eng. A*, 1989, **120–121**, 129–137, DOI: **10.1016/0921-5093(89)90730-2**.
50 K. Fritscher, The Reactive Element Effect, *Metall. Mater. Trans. A*, 2023, **54**, 64–74, DOI: **10.1007/s11661-022-06840-w**.
51 G. Akopov, M. T. Yeung and R. B. Kaner, Rediscovering the Crystal Chemistry of Borides, *Adv. Mater.*, 2017, **29**, 1604506, DOI: **10.1002/adma.201604506**.
52 M. M. Korsukova, V. N. Gurin, Y. B. Kuzma, N. F. Chaban, S. I. Chykhrii, V. V. Moshchalkov, N. B. Brandt, A. A. Gippius and K. K. Nyan, Crystal Structure, Electrical, and Magnetic Properties of the New Ternary Compounds $LnAlB_{14}$, *Phys. Status Solidi A*, 1989, **114**, 265–272, DOI: **10.1002/pssa.2211140126**.
53 S. M. Richards and K. J. S, The Crystal Structure of YB_{66}, *Acta Crystallogr.*, 1969, **B25**, 237–251, DOI: **10.1107/S056774086900207X**.
54 D. Berthebaud, A. Sato, Y. Michiue, T. Mori, A. Nomura, T. Shishido and K. Nakajima, Effect of Transition Element Doping on Crystal Structure of Rare Earth Borosilicides $REB_{44}Si_2$, *J. Solid State Chem.*, 2011, **184**, 1682–1687, DOI: **10.1016/j.jssc.2011.04.038**.
55 V. V. Odintsov, Hardness of Metal Dodecaborides of UB_{12} Structure Type, *Inorg. Chem.*, 1974, **10**, 366–367.
56 D. K. Das, Microstructure and High Temperature Oxidation Behavior of Pt-Modified Aluminide Bond Coats on Ni-base Superalloys, *Prog. Mater. Sci.*, 2013, **58**, 151–182, DOI: **10.1016/j.pmatsci.2012.08.002**.
57 Y. B. Kuz'ma, G. V. Chernyak, L. G. Akselrud, B. Y. Kotur and N. F. Chaban, The Crystal Structure of Boride Er_4NiB_{13} and its Analogs, *Kristallografiâ*, 1983, **28**, 1210–1212.
58 T. Konrad and W. Jeitschko, The Thorium Transition Metal Borides Th_2TB_{10} (T = Fe, Co, Ni) with a Structure very Similar to that of CaB_6, *Z. Naturforsch. B*, 1995, **50**, 1195–1199, DOI: **10.1515/znb-1995-0812**.
59 Y. B. Kuz'ma, Crystal Structure of the Compound $YCrB_4$ and its Analogs, *Sov. Phys. Crystallogr.*, 1970, **15**, 312–314.
60 Y. B. Kuz'ma and S. I. Svarichevskaya, Crystal Structure of Y_2ReB_6 and its Analogs, *Sov. Phys. Crystallogr.*, 1972, **17**, 569–571.
61 G. Akopov, H. Yin, I. Roh, L. E. Pangilinan and R. B. Kaner, Investigation of Hardness of Ternary Borides of the $YCrB_4$, Y_2ReB_6, Y_3ReB_7, and YMo_3B_7 Structural Types, *Chem. Mater.*, 2018, **30**, 6494–6502, DOI: **10.1021/acs.chemmater.8b03008**.
62 W. Jeitschko, T. Konrad, K. Hartjes, A. Lang and R.-D. Hoffmann, Polyborides with Th_2NiB_{10}-Type Structure: Synthesis, Crystal Structure, and Magnetic and Electrical Properties, *J. Solid State Chem.*, 2000, **154**, 246–253, DOI: **10.1006/jssc.2000.8844**.